




Design and Performance Analysis of Sparse TOPS SAR Mode

Hui Bi , *Member, IEEE*, Guoxu Li, Yufan Song, Jingjing Zhang , Daiyin Zhu ,
Wen Hong, *Senior Member, IEEE*, and Yirong Wu

I. INTRODUCTION

Abstract—Terrain observation by progressive scans (TOPS) is a novel and promising wide-swath synthetic aperture radar (SAR) imaging mode, which overcomes the scalloping effect existing in ScanSAR. Traditional imaging algorithms are computationally efficient in raw data processing of TOPS, but the problems from clutter and sidelobes suppression have not been effectively solved. Sparse SAR imaging not only effectively solves these problems, but also has great potential in improving system performance, e.g., lower requirement of pulse repetition frequency (PRF), higher swath coverage, less data amount, and lower system complexity. Therefore, this article proposes a novel sparse TOPS SAR imaging mode. The proposed mode combines advantages of sparse imaging system and TOPS mode to achieve high-quality and wide-swath SAR imaging. In this mode, we first design the beam position by timing diagram. Then, the basic parameters of the mode are calculated according to the radar equation, and the properties, such as grating lobes are analyzed. Finally, an $L_{2,1}$ -norm regularization based sparse TOPS SAR imaging algorithm is introduced to achieve the high-quality sparse scene recovery. Experimental results show that compared with conventional TOPS imaging mode, the proposed mode can obtain wide swath with lower PRF and effectively solve the effect on distributed target ambiguity ratio. Compared with matched filtering-based TOPS imaging algorithm, the sparse method can achieve unambiguous reconstruction of the considered scene from down-sampled data, and obtain the image with less artifacts.

Index Terms—Mode design, sparse synthetic aperture radar (SAR) imaging, SAR, terrain observation by progressive scans (TOPS).

Manuscript received 24 June 2022; revised 30 July 2022, 3 September 2022, and 18 September 2022; accepted 11 October 2022. Date of publication 14 October 2022; date of current version 21 October 2022. This work was supported in part by the National Natural Science Foundation of China under Grant 62271248 and Grant 61901213, in part by the Guangdong Basic and Applied Basic Research Foundation under Grant 2020B1515120060, in part by the Natural Science Foundation of Jiangsu Province under Grant BK20190397, in part by the Aeronautical Science Foundation of China under Grant 201920052001, in part by the Fundamental Research Funds for the Central Universities under Grant NE2020005, in part by the University Joint Innovation Fund Project of CALT under Grant CALT2021-11, and in part by the Science and Technology Innovation Project for Overseas Researchers in Nanjing. (*Corresponding author: Hui Bi.*)

Hui Bi, Guoxu Li, Yufan Song, Jingjing Zhang, and Daiyin Zhu are with the Key Laboratory of Radar Imaging and Microwave Photonics, Ministry of Education, Nanjing University of Aeronautics and Astronautics, Nanjing 211106, China, and also with the College of Electronic and Information Engineering, Nanjing University of Aeronautics and Astronautics, Nanjing 211106, China (e-mail: bihui@nuaa.edu.cn; c31644916@126.com; songyufan@nuaa.edu.cn; jingjingzhang@nuaa.edu.cn; zhudy@nuaa.edu.cn).

Wen Hong and Yirong Wu are with the Aerospace Information Research Institute, Chinese Academy of Sciences, Beijing 100094, China (e-mail: hong@mail.ie.ac.cn; wyr@mail.ie.ac.cn).

Digital Object Identifier 10.1109/JSTARS.2022.3214514

AS A main technology of modern remote sensing, synthetic aperture radar (SAR) is a kind of high-resolution imaging system, which has been widely used in military and civilian fields [1]. SAR systems usually focus on two key performance indicators: high-resolution and wide-swath. However, high-resolution and wide-swath are a pair of contradictories due to the conflicting requirements on pulse repetition frequency (PRF), i.e., wider swath requires lower PRF, but low PRF limits the increase of resolution [2]. In recent years, several methods have been proposed to solve the contradiction between high-resolution and wide-swath [3]. These methods are divided into two main categories. One class of methods is based on multi-channel techniques, e.g., displaced phase center antenna [4], [5]. It aims to improve mapping capability by breaking the contradiction between resolution and swath width. However, these methods require high ability of data processing and power consumption. The other category is SAR imaging mode design. It makes a tradeoff between resolution and swath width by beam scanning. Different working modes have different resolution and swath coverage. Spotlight mode provides long-term observation of an area by sacrificing azimuth swath width, which can achieve the purpose of high-resolution observation [6], [7]. By beam switching among the subswaths, ScanSAR sacrifices resolution to obtain swath coverage [8], [9]. These two modes have gradually developed into main working schemes of spaceborne SAR. Based on them, several working modes have been developed such as terrain observation by progressive scans (TOPS) [10], [11] and sliding spotlight [12], [13]. TOPS is a novel burst imaging mode, which is proposed to solve the wide-swath imaging problem [14]. It can improve observation scope by beam switching among the subswaths in range direction [15]. All targets are illuminated with antenna azimuth pattern (AAP) by scanning beam in azimuth direction [16]. Therefore, TOPS can achieve the same swath coverage compared to ScanSAR, but with greatly reduced scalloping [17], [18].

As a well-known matched filtering (MF) based SAR imaging algorithm, chirp scaling [19], [20] has been widely used in the imaging process of different SAR working modes [21], [22], [23]. For ScanSAR, Moreira et al. [24] proposed an extended chirp scaling (ECS) algorithm, which utilizes spectral analysis technique to achieve azimuth scaling. Prats et al. [25] proposed a ECS-based baseband azimuth scaling algorithm, which obtains high-quality TOPS SAR image by using subaperture technique.

Xu et al. [26] introduced a two-step algorithm to process TOPS echo data, which avoids subaperture division operations. In recent years, several MF-based imaging algorithms have been developed for TOPS raw data processing [27], [28], [29], [30]. However, the problems of clutter and sidelobe suppression remain unsolved, which limit the development of target recognition, feature acquisition, etc. Sparse signal processing theory was proposed in 1990s, which can recover the sparse signal from fewer samples [31]. Then, Donoho et al. [32] proposed compressive sensing (CS) theory, which is an important development of sparse signal processing technology [33]. According to CS, if measurement matrix satisfies some conditions, such as restricted isometry property [36], the sparse scene can be perfectly recovered from fewer samples than the Shannon–Nyquist sampling theory required [34], [35], [36]. After introducing sparse signal processing technique into SAR imaging, a novel sparse SAR imaging theory was formed. Zhang et al. proposed an azimuth-range decouple-based L_q -norm regularization SAR imaging method. Compared with conventional observation matrix based sparse imaging method, it can dramatically reduce the computational complexity and allow the practical large-scale sparse scene reconstruction [37]. Then, this idea is applied in the the data processing of different SAR modes, e.g., Stripmap [37], Scan [38], [39], and Sliding Spotlight [40]. Wang et al. [41] achieved extremely high-resolution in sliding spotlight SAR by designing continuously varying pulse interval sequence. Moreover, Bi et al. [42] proposed an L_1 -norm regularization based TOPS SAR sparse imaging method, and achieved large-scale high-quality sparse recovery with less computational cost.

Compared with typical SAR imaging system, sparse SAR imaging system has lower complexity and better performance, such as lower requirement of PRF, wider swath, and better target distinguishing ability, and provides an alternative for high-resolution wide-swath microwave imaging [43]. In addition, compared with MF, sparse SAR imaging method shows better imaging ability when the number of samples in the echo data is too small (collected by low PRF), and achieves unambiguous sparse recovery of large-scale region with lower sidelobes and higher signal-to-clutter-noise ratio [44].

In this article, we propose a novel sparse TOPS SAR imaging mode that combines the advantages of sparse imaging and TOPS. This mode first designs beam positions through the timing diagram. Then, we calculate the indispensable parameters of sparse TOPS SAR based on the radar equation, and analyze the performance, such as grating lobes by AAP. Finally, an $L_{2,1}$ -norm regularization based sparse TOPS SAR imaging method is introduced to the scene recovery of the designed sparse mode, and achieves the high-quality sparse reconstruction of considered scene with less azimuth ambiguity by introducing the ambiguity terms into the sparse imaging model. Compared with traditional TOPS mode, sparse TOPS mode uses beam position obtained by down-sampling, and uses the proposed sparse imaging method rather than MF-based imaging method for scene recovery. Without changing the other system parameters of traditional TOPS mode, it can extend swath width by reducing PRF. In order to validate superiority of the proposed imaging mode, this article compares system performance and imaging

performance of sparse and conventional TOPS, respectively. In the comparison of system performance, we analyze the azimuth ambiguity to signal ratio (AASR), signal-to-noise ratio (SNR), and distributed target ambiguity ratio (DTAR). In the imaging performance, we compare the proposed sparse imaging method and MF based algorithm in terms of sidelobe reduction, noise and clutter suppression, and down-sampling imaging ability. Experimental results based on TerraSAR-X satellite parameters show that compared with typical TOPS mode, the proposed sparse imaging mode can increase the swath coverage from 120 to 160 km and effectively suppress the effect of steering angle on DTAR. Unlike typical MF, the proposed sparse imaging method can achieve unambiguous imaging of the designed sparse TOPS mode, which makes it possible to obtain wider swath with lower PRF, enabling high-quality and wide-swath imaging.

The rest of this article is organized as follows. Section II provides a brief introduction of the basic principle of TOPS mode. Section III introduces the design principle of the proposed mode in detail including beam position design, parameter calculation, and grating lobes analysis. The proposed $L_{2,1}$ -norm regularization based sparse TOPS SAR imaging algorithm is discussed in Section IV. Section V shows the performance analysis of the designed sparse TOPS SAR imaging system. Experimental results based on simulated and real data are provided in Section VI to support our viewpoint. Finally, Section VII concludes this article.

II. TOPS SAR IMAGING MODE

In TOPS mode, the antenna beam is steered in azimuth and range directions. Similar to ScanSAR, the swath coverage is divided into different subswaths and antenna beam is periodically switched between subswaths. The antenna beam is scanned from aft to fore in azimuth direction. It should be noted that the rotation center of antenna is opposite to spotlight. Thus, the azimuth resolution will be worse in TOPS mode. The imaging geometry of TOPS SAR is shown in Fig. 1. The steering angle can be expressed as

$$\phi(t) = |k_\phi| t, \quad k_\phi \leq 0 \quad (1)$$

where k_ϕ (rad/s) is the antenna steering angle rate, and t is the azimuth slow time. According to [10] and [11], the azimuth antenna pattern of TOPS can be written as

$$\begin{aligned} G_T(\phi(t)) &= \text{sinc}^2 \left(\frac{L_a}{\lambda} \cdot \left(\frac{v_g t}{R_0} + \phi(t) \right) \right) \\ &= \text{sinc}^2 \left(\frac{L_a v_g t}{\lambda R_0} \cdot \left(1 + \frac{R_0 |k_\phi|}{v_g} \right) \right) \end{aligned} \quad (2)$$

where v_g is the beam ground velocity, R_0 is the range of closest approach, λ is the wavelength, and L_a is the length of azimuth antenna. Compared with stripmap mode, the azimuth resolution of TOPS is reduced by a factor

$$\alpha = 1 + \frac{R_0 |k_\phi|}{v_g} \quad (3)$$

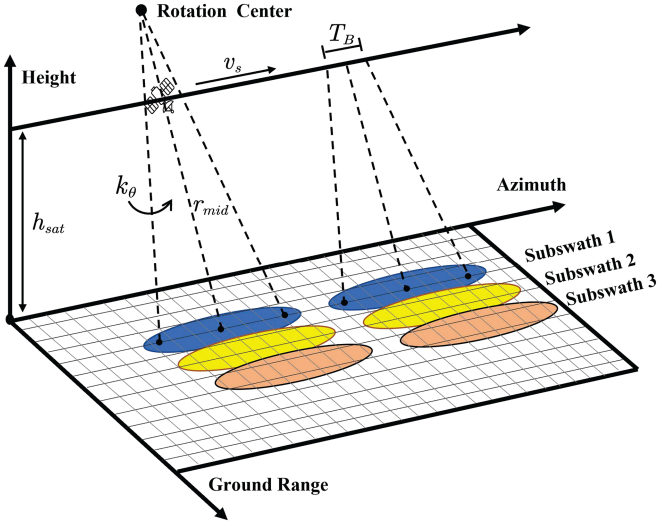


Fig. 1. TOPS SAR acquisition geometry.

and can be expressed as

$$\rho_{az} = \frac{\lambda \alpha}{2\phi_0} \quad (4)$$

where ϕ_0 is the azimuth beamwidth. Therefore, the target illumination time is reduced. If the value of the antenna azimuth bandwidth is fixed, the steering angle rate for each subswath can be derived as

$$|k_\phi^n| = \left(\frac{2\rho_{az}\phi_0^n}{\lambda} - 1 \right) \frac{v_g^n}{R_0^n} \quad (5)$$

where n is the n th subswath. To ensure continuous coverage of the different subswaths, the equations must be satisfied

$$(|k_\phi^n| T_B^n - \phi_0^n) R_0^n + v_g^n T_B^n = v_g^n T_R \quad (6)$$

$$T_R = \sum_n T_B^n + T_G^n \quad (7)$$

where T_B is the burst time, T_R is the cycle time, and T_G is the time used to switch between different subswaths.

III. SPARSE TOPS SAR IMAGING MODE

A. Beam Position Design

In sparse TOPS SAR imaging mode, we first design beam position by timing diagram. Then, the essential parameters are calculated based on the radar equation. Finally, the grating lobes are analyzed by AAP. It should be noted that the basic parameters used for mode design are based on TOPS mode of TerraSAR-X satellite [11]. The main parameters of TerraSAR-X are listed in Table I. The selection of beam position is important to improve system performance. In the beam position design of sparse TOPS, the PRF is reduced to 75% of the original. The choice of PRF must take into account the limitations of transmit and nadir interference. The timing diagram is depicted in Fig. 2, which shows the range of incidence angles for four subswaths in sparse TOPS and conventional TOPS modes, respectively. It is seen that compared with conventional TOPS, the PRF of

TABLE I
TERRASAR-X PARAMETERS

Carrier frequency	9.65 GHz
Azimuth antenna length	4.8 m
Azimuth beamwidth	0.33°
Platform high	514 km
Platform velocity	7608 m/s
Maximum steering capability	0.75°
Number of subswaths	4
Azimuth resolution	16 m
Azimuth TR modules	12

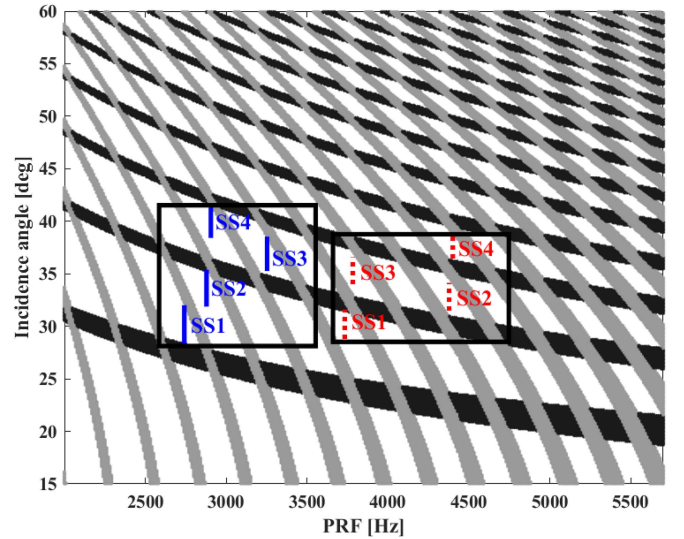


Fig. 2. Timing diagram of four subswaths in TOPS mode. (The solid blue line on the left is the sparse TOPS, and the dashed red line on the right is the conventional TOPS.)

sparse TOPS decreases from 3700–4400 Hz to 2700–3000 Hz, but incidence angle increases from 10.09° to 13.21°. Therefore, the incident angle range of the four subswaths in sparse TOPS is significantly larger than that in TOPS SAR. This means that the swath coverage of sparse TOPS mode will increase.

B. Parameter Calculation

According to the timing diagram in Fig. 2, we calculate the essential system parameters of sparse and conventional TOPS modes, respectively (see Table II). Without loss of generality, we select subswath 1 (SS1) as the example to compare two TOPS modes. From Table II, it is seen that SS1 of conventional TOPS has 30.12 km swath width with PRF = 3732 Hz. While in the designed sparse TOPS, PRF of SS1 is reduced to PRF = 2741 Hz, and obtained the 40.17 km swath width. It is found that in sparse TOPS, when the PRF is reduced to 75% of original, the swath coverage of each subswath will increase from 30 to 40 km. This increases the total swath width from 120 to 160 km without changing to other parameters such as azimuth resolution and beamwidth.

TABLE II
PARAMETERS OF DESIGNED SPARSE TOPS SAR IMAGING MODE AND
CONVENTIONAL TOPS SAR IMAGING MODE

	SS1	SS2	SS3	SS4
Sparse TOPS SAR imaging mode				
PRF [Hz]	2741	2878	3252	2905
Incident angle (near) [deg]	28.26	31.88	35.26	38.41
Incident angle (far) [deg]	32.01	35.39	38.54	41.47
Middle look angle [deg]	27.67	30.83	33.75	36.44
Slant middle range [km]	586.9	607.4	629.7	653.6
Azimuth resolution [m]	16	16	16	16
Beamwidth [deg]	0.33	0.33	0.33	0.33
Effective radar velocity [m/s]	7315	7314	7313	7312
Ground velocity [m/s]	7034	7032	7030	7027
Subswath width [km]	40.17	40.13	40.15	40.18
Total swath width [km]	~ 160			
Conventional TOPS SAR imaging mode				
PRF [Hz]	3732	4377	3782	4400
Incident angle (near) [deg]	28.78	31.46	34.01	36.44
Incident angle (far) [deg]	31.59	34.14	36.57	38.87
Middle look angle [deg]	27.74	30.10	32.33	34.44
Slant middle range [km]	582.8	597.6	613.6	630.5
Azimuth resolution [m]	16	16	16	16
Beamwidth [deg]	0.33	0.33	0.33	0.33
Effective radar velocity [m/s]	7315	7314	7313	7313
Ground velocity [m/s]	7034	7032	7031	7029
Subswath width [km]	30.12	30.14	30.26	30.24
Total swath width [km]	~ 120			

C. Grating Lobes Analysis

In order to realize the antenna beam scanning in both azimuth and range directions, the planar phased array antenna adopts the TOPS mode. According to [4], the two-way azimuth antenna pattern of the entire antenna can be written as

$$G_{2w}(\theta, t) = G_T(\theta, t) \cdot G_R(\theta, t) \quad (8)$$

where $G_T(\theta, t)$ and $G_R(\theta, t)$ are the transmit and receive azimuth antenna pattern, i.e.,

$$G_T(\theta, t) = \sqrt{G_e} \left| \frac{1}{M} \sum_{k=0}^{M-1} C_{k,T} \exp \left(j \frac{2\pi k}{\lambda} L_e \sin \theta \right) \right|$$

$$G_R(\theta, t) = \sqrt{G_e} \left| \frac{1}{M} \sum_{k=0}^{M-1} C_{k,R} \exp \left(j \frac{2\pi k}{\lambda} L_e \sin \theta \right) \right| \quad (9)$$

with

$$G_e(\theta) = \text{sinc}^2 \left(\frac{L_e}{\lambda} \sin \theta \right) \quad (10)$$

$$C_{k,T} = a_{k,T} \exp \left(j \frac{2\pi k}{\lambda} L_e \sin \phi(t) \right) \quad (11)$$

$$C_{k,R} = a_{k,R} \exp \left(j \frac{2\pi k}{\lambda} L_e \sin \phi(t - \Delta t) \right) \quad (12)$$

where G_e is the antenna pattern of single element, M is the number of T/R modules, L_e is the length of single element, $C_{k,T}$ and $C_{k,R}$ are the transmit and receive excitation coefficients, $a_{k,T}$ and $a_{k,R}$ are the amplitude of $C_{k,T}$ and $C_{k,R}$, and Δt is the delay time. The grating lobes can be analyzed by the two-way azimuth antenna pattern. According to (8)–(12), it can be concluded that the steering angle affects the AAP in TOPS mode. AAP is plotted in Fig. 3. The total AAP is the result of weighting the array antenna pattern and the single antenna azimuth element pattern. As shown in Fig. 3, it is seen that the sidelobes is proportional to the steering angle, i.e., sidelobes increases with the steering angle, and can even reach the mainlobe. Therefore, DTAR is affected by the steering angle. In practice, we expect DTAR to be independent of steering angle to ensure stable image quality. Sparse TOPS SAR imaging mode can effectively suppress this phenomenon, which will be presented in Section V.

IV. $L_{2,1}$ -NORM REGULARIZATION BASED SPARSE TOPS SAR IMAGING

A. Two-Step TOPS SAR Imaging Algorithm

The echo of TOPS has both ScanSAR and spotlight echo characteristics, i.e., azimuth data folding and Doppler spectrum aliasing. Two-step processing approach can solve this problem to obtain the focused image by using azimuth preprocessing and postprocessing operations. The echo data $y(t, \tau)$ of TOPS SAR can be written as

$$y(t, \tau) = \iint_{(p,q)} x(p, q) \text{rect} \left(\frac{t}{T_B} \right) \omega_a \left(\frac{t - p/v - t_c(t)}{T_s} \right) \cdot \exp \left\{ -j \frac{4\pi}{\lambda} R \right\} s \left(\tau - \frac{2R}{c} \right) dpdq \quad (13)$$

where t is the azimuth time, τ is the range time, p is the target azimuth position, q is the target range position, $x(p, q)$ is the backscattered coefficient at position (p, q) , $\omega_a(\cdot)$ is the antenna azimuth weighting, c is the light speed, v is the platform velocity, T_s is the synthetic aperture time, $t_c(t)$ is the beam center cross time, and R is the slant range. The flow diagram of two-step processing algorithm is shown in Fig. 4, including azimuth preprocessing, chirp scaling, and azimuth postprocessing. In azimuth preprocessing, the convolution operation between linear frequency modulation (FM) signals consisted of one fast Fourier transform (FFT) operation and two function multiplication. The selected reference linear FM signal \mathbf{H}_1 is

$$\mathbf{H}_1(t) = \exp \left\{ j\pi \frac{2v^2}{\lambda R_r} t^2 \right\} \cdot \exp \{ j2\pi f_{dc} t \} \quad (14)$$

where R_r is the reference slant range, and f_{dc} is the target Doppler center frequency in scene center. The second term in (14) is used to remove scene Doppler center to avoid Doppler spectrum aliasing caused by azimuth convolution. After FFT, the azimuth preprocessing is completed by multiplying transfer function

$$\mathbf{H}_2(t') = \exp \left\{ j\pi \frac{2v^2}{\lambda R_r} t'^2 \right\} \quad (15)$$

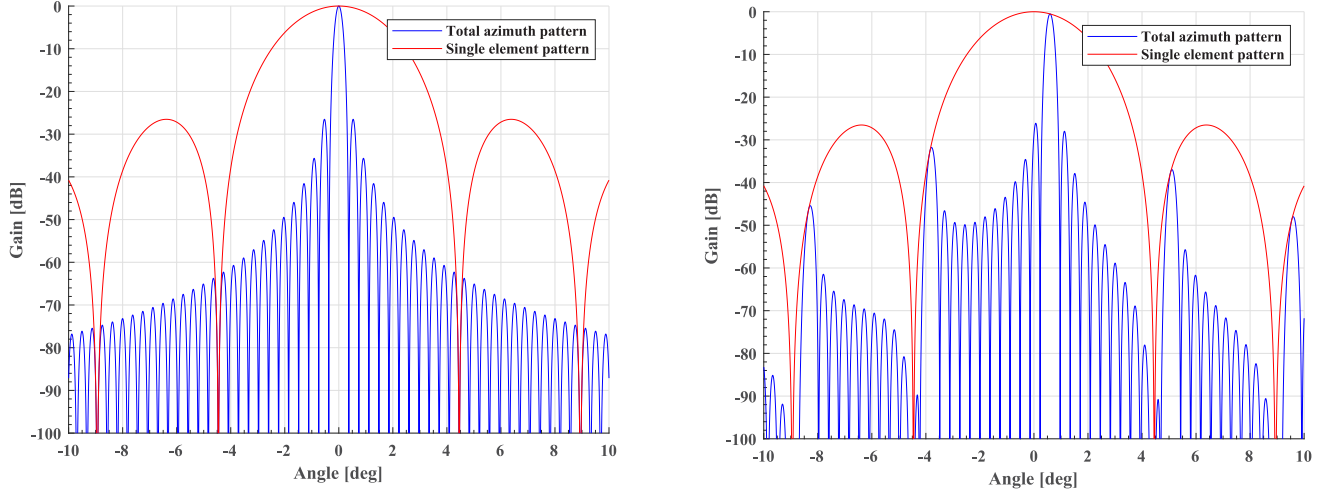


Fig. 3. Element and total azimuth antenna pattern. (a) Steering angle equals to 0° . (b) Steering angle equals to 0.6° .

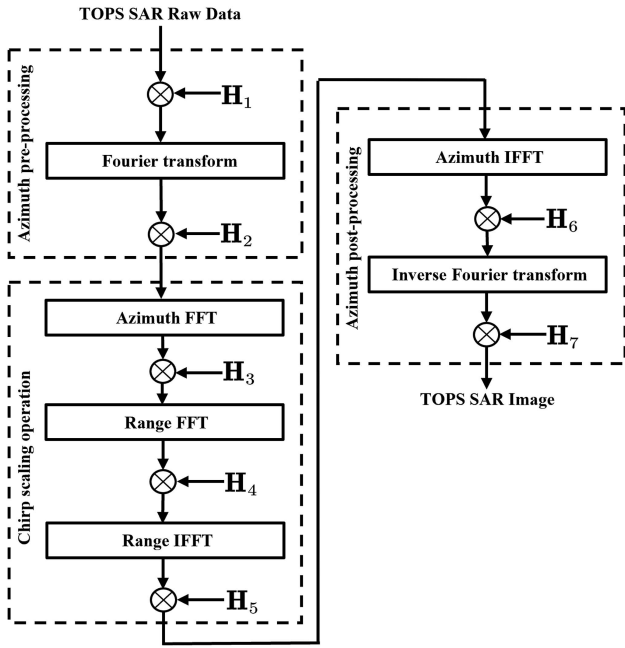


Fig. 4. Flow diagram of two-step algorithm.

where t' is the azimuth time after zero-padding.

After abovementioned operations, the problem of Doppler spectrum aliasing is solved. Then, the echo data Doppler history is recovered by \mathbf{H}_3 , i.e.,

$$\mathbf{H}_3(f'_t) = \exp \left\{ j\pi \frac{\lambda R_r}{2v^2} f_t'^2 \right\} \quad (16)$$

where f'_t is the azimuth frequency. Next, range compression and consistent range cell migration correction will be implemented in the 2-D frequency domain by multiplying

$$\mathbf{H}_4(f_t, f_\tau) = \exp \left\{ j\pi \frac{f_\tau^2}{K_m(f_t, f_\tau)} \right\}$$

$$\cdot \exp \left\{ j \frac{4\pi R_0 (1 - D(f_t, f_\tau))}{cD(f_t, f_\tau)} f_\tau \right\} \quad (17)$$

where f_τ is the range frequency, and $K_m(f_t, f_\tau)$ is the modified modulation rate of chirp signal, i.e.,

$$K_m(f_t, f_\tau) = \frac{K_r}{1 - K_r/K_{src}(f_t, f_\tau)} \quad (18)$$

with

$$K_{src}(f_t, f_\tau) = \frac{2v^2 f_0^3 D(f_t, f_\tau)^3}{cR_0 f_t^2} \quad (19)$$

$$D(f_t, f_\tau) = \sqrt{1 - \left(\frac{c f_t'}{2v(f_0 + f_\tau)} \right)^2} \quad (20)$$

where K_r is the modulation rate, and f_0 is the carrier frequency. After that, azimuth compression and solution of azimuth data folding will be completed by multiplying

$$\mathbf{H}_5(f'_t) = \exp \left\{ j4\pi \frac{R_0 \beta(f'_t) f_0}{c} \right\} \cdot \exp \left\{ j\pi \frac{f_t'^2}{k_d} \right\} \quad (21)$$

with

$$\beta(f'_t) = \sqrt{1 - \left(\frac{c f_t'}{2v f_0} \right)^2} \quad (22)$$

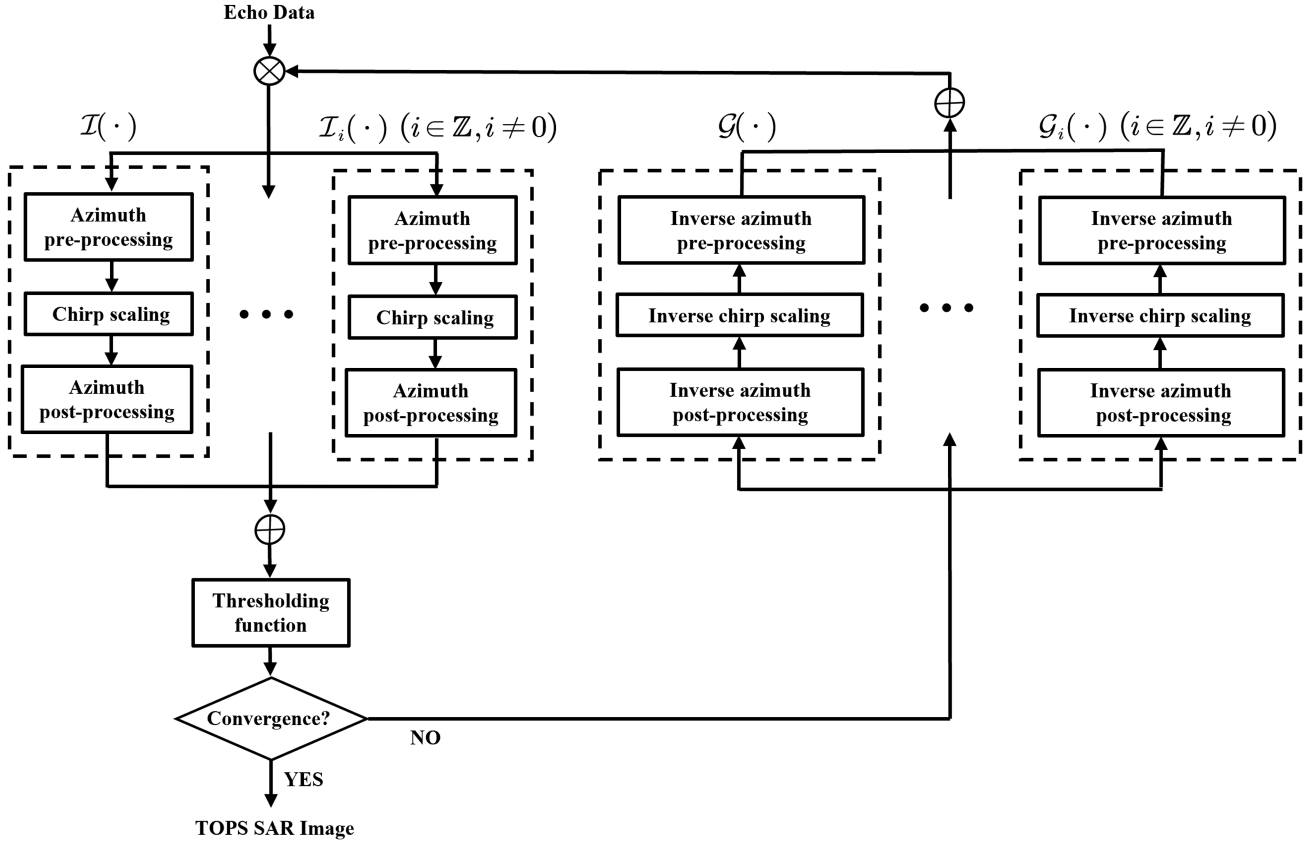
where k_d is the modulation rate of reference signal, which can be expressed as

$$k_d = \frac{2v^2}{\lambda (R_r + R_0)}. \quad (23)$$

Finally, $\mathbf{H}_6(f_t'')$ and $\mathbf{H}_7(t'')$ are used for azimuth postprocessing operation to obtain focused TOPS SAR imaging and can be written as

$$\mathbf{H}_6(f_t'') = \exp \left\{ j\pi \frac{f_t''^2}{k_d} \right\} \quad (24)$$

$$\mathbf{H}_7(t'') = \exp \left\{ j\pi k_d (t'' - t_{\text{mid}})^2 \right\} \quad (25)$$


 Fig. 5. Flow diagram of the proposed $L_{2,1}$ -norm regularization-based sparse TOPS imaging algorithm.

where t'' and f_t'' are the azimuth time and frequency after intercept operation, and t_{mid} is the scene center time.

B. $L_{2,1}$ -Norm Regularization-Based Sparse TOPS SAR Imaging Algorithm

Let $\mathbf{X} \in \mathbb{C}^{N_P \times N_Q}$ denotes the backscattered coefficient of the surveillance region with N_P and N_Q being the number of points in azimuth and range directions, respectively, $\mathbf{Y} \in \mathbb{C}^{N_t \times N_r}$ denotes the 2-D echo data, $\mathcal{I}(\cdot)$ and $\mathcal{G}(\cdot)$ represent the imaging and inverse imaging operators in above discussed two-step TOPS SAR imaging algorithm, respectively. Then, we have

$$\begin{aligned} \mathcal{I}(\mathbf{Y}) = & \mathbf{F}^{-1} \{ \mathbf{F}_a^{-1} [\mathbf{F}_a (\mathbf{F}(\mathbf{Y} \circ \mathbf{H}_1) \circ \mathbf{H}_2) \\ & \circ \mathbf{H}_3 \mathbf{F}_r \circ \mathbf{H}_4 \mathbf{F}_r^{-1} \circ \mathbf{H}_5] \circ \mathbf{H}_6 \} \circ \mathbf{H}_7 \end{aligned} \quad (26)$$

$$\begin{aligned} \mathcal{G}(\mathbf{X}) = & \mathbf{F}^{-1} \{ \mathbf{F}_a^{-1} [\mathbf{F}_a (\mathbf{F}(\mathbf{X} \circ \mathbf{H}_7^H) \circ \mathbf{H}_6^H) \\ & \circ \mathbf{H}_5^H \mathbf{F}_r \circ \mathbf{H}_4^H \mathbf{F}_r^{-1} \circ \mathbf{H}_3^H] \circ \mathbf{H}_2^H \} \circ \mathbf{H}_1^H \end{aligned} \quad (27)$$

where \mathbf{F}_a is azimuth Fourier transform, \mathbf{F}_r is range Fourier transform, \mathbf{F} denotes Fourier transform in azimuth preprocessing operation, \mathbf{F}_a^{-1} , \mathbf{F}_r^{-1} , and \mathbf{F}^{-1} are the inverse processes of \mathbf{F}_a , \mathbf{F}_r , and \mathbf{F} , \circ is the Hadamard product operation.

Then, we can write the 2-D sparse TOPS SAR imaging model as [46]

$$\mathbf{Y} = \mathbf{\Xi} \circ \left(\mathcal{G}(\mathbf{X}) + \sum_i \mathcal{G}_i(\mathbf{X}_i) \right) + \mathbf{N}, i \in \mathbb{Z}, i \neq 0 \quad (28)$$

where $\mathbf{\Xi}$ is the down-sampling matrix, $\mathcal{G}_i(\cdot)$ denotes the inverse imaging operators for ambiguity areas, $\mathbf{X}_i \in \mathbb{C}^{N_P \times N_Q}$ with $i \in \mathbb{Z}^-$ and $i \in \mathbb{Z}^+$ denote the left and right ambiguity areas, and \mathbf{N} is the noise matrix. According to the model in (28), we can reconstruct the considered scene by solving the $L_{2,1}$ -norm regularization problem

$$\begin{aligned} \hat{\mathbf{X}} = \min_{\mathbf{X}} \left\{ \left\| \mathbf{Y} - \mathbf{\Xi} \circ \left(\mathcal{G}(\mathbf{X}) + \sum_i \mathcal{G}_i(\mathbf{X}_i) \right) \right\|_F^2 \right. \\ \left. + \beta_1 \|\mathbf{X}_{\text{all}}\|_{2,1}^1 + \beta_2 \|\mathbf{X}\|_1 \right\} \end{aligned} \quad (29)$$

where $\hat{\mathbf{X}}$ is the reconstructed image of considered scene, β_2 is the regularization parameter which controls the sparsity of \mathbf{X} , and β_1 controls the sparsity of the whole scene \mathbf{X}_{all} , which can be expressed as

$$\|\mathbf{X}_{\text{all}}\|_{2,1}^1 = \left(\sum_{np=1}^{N_P} \left(\|\mathbf{X}_{np}\|_F + \sum_i \|\mathbf{X}_{i,np}\|_F \right) \right). \quad (30)$$

where \mathbf{X}_{np} and $\mathbf{X}_{i,np}$ are the np th row of \mathbf{X} and \mathbf{X}_i , respectively, and $np = 1, 2, \dots, N_P$. For the optimization problem in (29),

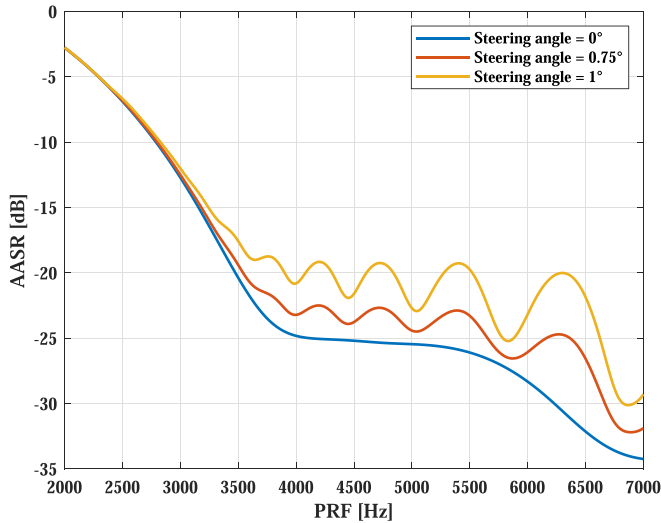


Fig. 6. Relationship between AASR and PRF under different steering angles.

we can use the iterative soft thresholding (IST) algorithm to obtain the focused sparse image. The detailed iterative flow of IST is listed in Fig. 5 [42], [46].

C. Computational Cost Analysis

Let I denotes the number of required iterative steps for the accurate reconstruction of the proposed L_1 -norm regularization based sparse TOPS imaging algorithm. $M = N_t \times N_\tau$ and $N = N_P \times N_Q$ represent the number of points in the echo data and discretized surveillance scene. Then, the computational complexity of the two-step imaging method can be expressed as $\mathcal{O}(M \log(M))$ [42]. For each iteration of the proposed method, its computation includes two main parts, i.e., the calculations of an inverse MF and an MF procedure, which has the complexity of $\mathcal{O}(M \log(M))$, and a thresholding operation with the complexity $\mathcal{O}(N)$. Thus, its total computational complexity is in the order of $\mathcal{O}(I(M \log(M) + N))$ [42], [45]. Since the proposed algorithm usually converges within 10 steps, e.g., $I \leq 10$, it means that it has similar computational complexity to traditional MF-based imaging methods, which makes sparse reconstruction of large-scale scene possible.

V. SYSTEM PERFORMANCE ANALYSIS

In this section, the relationship between AASR and PRF, DTAR versus steering angle and beamwidth, and SNR versus beamwidth were used to analyze the system performance. The relationship between AASR and PRF is shown in Fig. 6. It is seen that AASR is inversely proportional to PRF, i.e., AASR will decrease as PRF increases. In addition, it is found that the larger steering angle, the larger change of AASR, and this change becomes more and more obvious with the increase of PRF. In sparse TOPS, when PRF is reduced to 75% of original one (see Table II), the AASR increases by about 13 dB. This means that we need to pay more attention in the following sparse imaging process to reduce the influence of steering angle on AASR

by sparse sampling in the azimuth direction. The relationship between DTAR and steering angle is shown in Fig. 7. In Fig. 7(a), we can see that when the steering angle is 0.6° , the DTAR of sparse TOPS does not change much. When steering angle equals to 1° , the maximum change of DTAR is about 2.3 dB. In conventional TOPS, when steering angle is greater than 0.6° , its effect on DTAR becomes more and more obvious. DTAR deteriorates by more than 5 dB when steering angle reaches 1° [see Fig. 7(b)]. From Fig. 7, we can conclude that sparse TOPS effectively suppresses the problem of DTAR varying with steering angle. This means that compared with conventional TOPS, sparse TOPS SAR imaging mode can obtain more stable image quality. Fig. 8 shows the relationship between DTAR and beamwidth. In sparse TOPS, as shown in Fig. 8(a), it is seen that when the beamwidth changes from 0.23° to 0.39° , the DTAR varies by about 10 dB. But in conventional TOPS, DTAR hardly varies with beamwidth [see Fig. 8(b)]. This indicates that the effect of beamwidth on DTAR becomes obvious when PRF decreases. Thus, we have to consider the effect of beamwidth on DTAR in sparse TOPS design. The relationship between SNR and beamwidth is shown in Fig. 9. In sparse TOPS, when beamwidth changes from 0.25° to 0.4° , the SNR decreases 2 dB. The same beamwidth change in conventional TOPS leads to 1.6 dB variation of SNR. Thus beamwidth variation has little effect on SNR in both modes.

In summary, compared with conventional TOPS, the designed sparse TOPS SAR imaging mode can effectively suppress the effect of steering angle on DTAR. But beamwidth in sparse TOPS has significant effect on DTAR. Therefore, the influence of beamwidth should be considered in the mode design.

VI. EXPERIMENTAL RESULT OF DESIGNED MODE

A. Point Target Simulation

In the following, several experiments based on simulated echo of point targets are performed to validate the superior performance of the designed sparse TOPS mode. Three point targets, named as T1, T2, T3 are located at $(R_c - 1000 \text{ m}, -4587 \text{ m})$, $(R_c, 0)$, and $(R_c + 1000 \text{ m}, 4587 \text{ m})$, respectively. Experimental parameters are set according to Table II. Fig. 10(a) and (b) shows the reconstructed results of T2 by two-step algorithm and the proposed sparse TOPS SAR imaging method in conventional TOPS mode. It is seen that when there is no down-sampling of echo data, both MF-based algorithm and sparse method can obtain the well focused point target, just the sparse recovered image has the lower sidelobes. Then, we add some noise and clutter to the simulated echo data and reconstruct the point targets by two-step algorithm and the sparse imaging method, respectively. The contour plots of T2 are shown in Fig. 10(c) and (d). It is can be seen that compared with MF-based result, the image recovered by the sparse method has better quality with less noise and clutter and reduced sidelobes. Fig. 11 shows the reconstructed images by two-step algorithm and the proposed sparse imaging method in conventional TOPS and designed sparse TOPS modes, respectively.

In Fig. 11(a) and (b), we can see that both two methods can obtain focused point targets. Fig. 11(c) shows that due to the

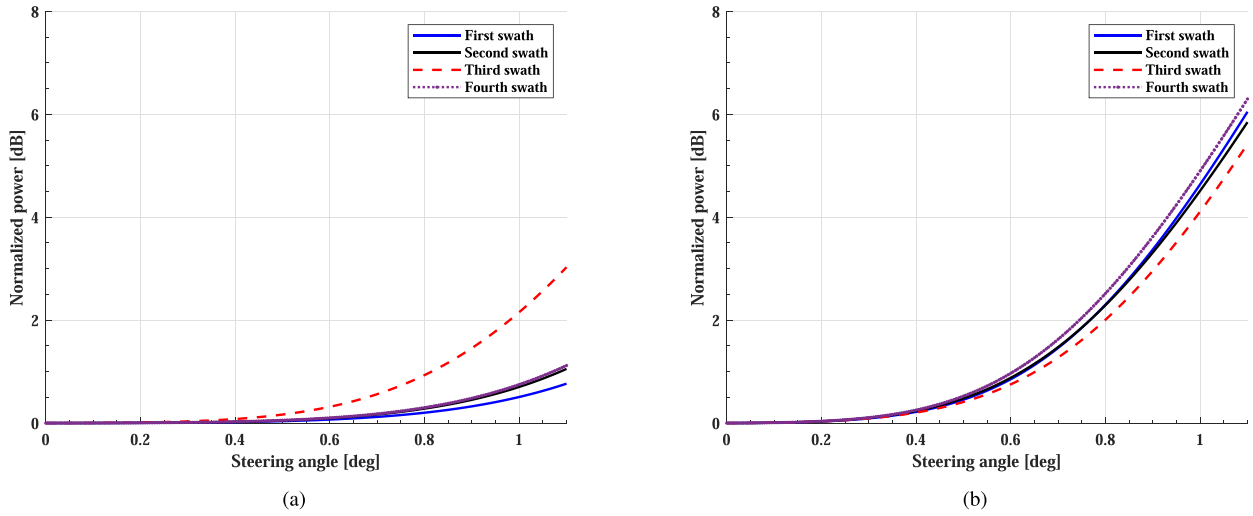


Fig. 7. Relationship between DTAR and steering angle (the power loss is normalized to the boresight case). (a) Performance of four subswaths in sparse TOPS mode. (b) Performance of four subswaths in conventional TOPS mode.

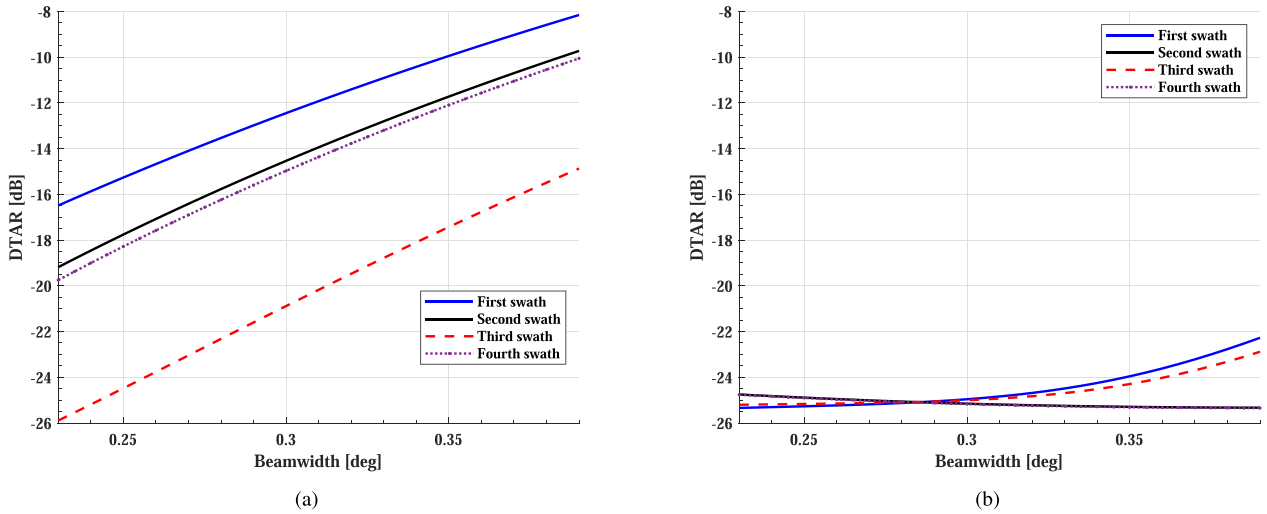


Fig. 8. Relationship between DTAR and beamwidth. (a) Performance of four subswaths in sparse TOPS mode. (b) Performance of four subswaths in conventional TOPS mode.

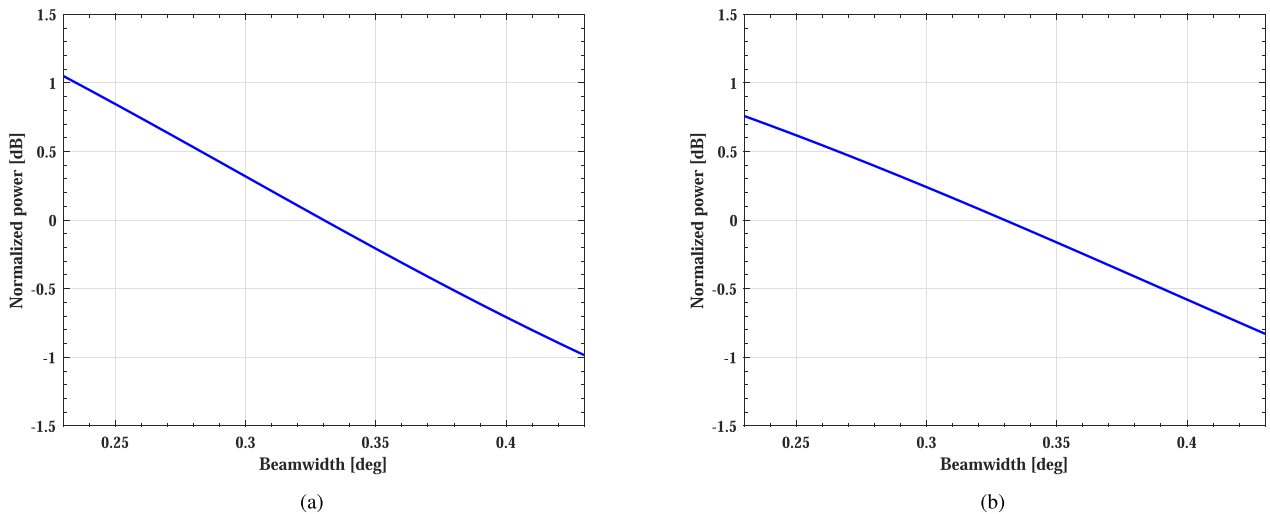


Fig. 9. Relationship between SNR and beamwidth (the value of SNR is normalized by the beamwidth equal to 0.33°). (a) Sparse TOPS mode. (b) Conventional TOPS mode.

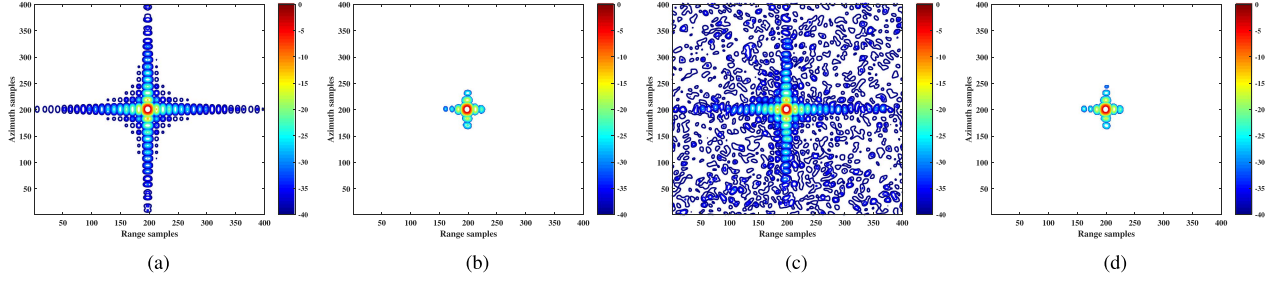


Fig. 10. Reconstructed images of T2 by different methods (in dB). (a) Two-step algorithm (MF). (b) Proposed $L_{2,1}$ -norm regularization based sparse imaging method. (c) Two-step algorithm with noise and clutter. (d) Proposed $L_{2,1}$ -norm regularization based sparse imaging method with noise and clutter.

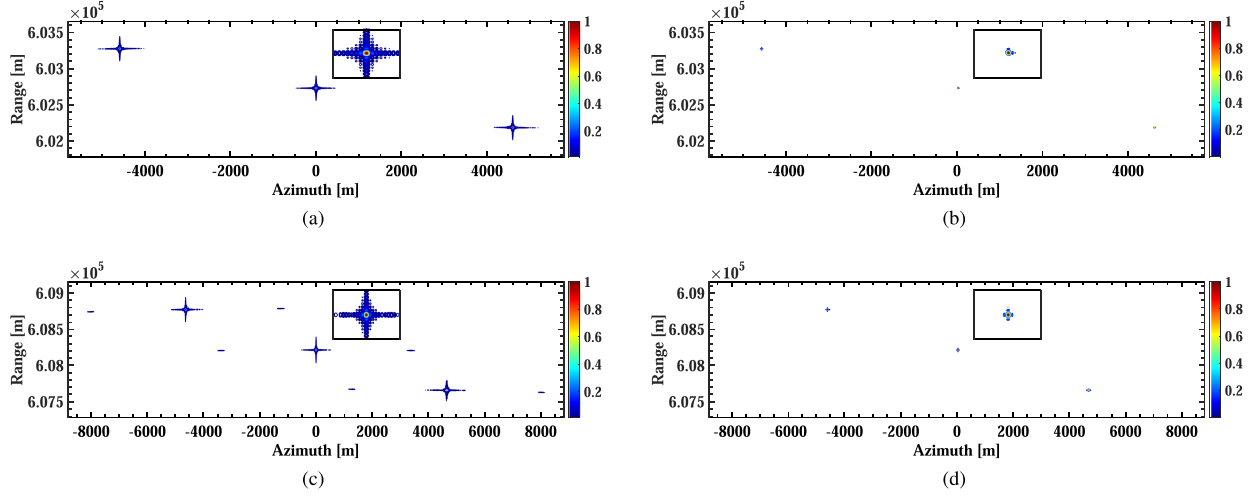


Fig. 11. Reconstructed images of point targets by different methods. (a) Two-step algorithm in conventional TOPS mode. (b) Proposed $L_{2,1}$ -norm regularization-based sparse imaging method in conventional TOPS mode. (c) Two-step algorithm in sparse TOPS mode. (d) Proposed $L_{2,1}$ -norm regularization based sparse imaging method in sparse TOPS mode.

down-sampled data, typical MF-based imaging algorithm can no longer recover the targets. Its recovered images show obvious periodic ambiguities along the azimuth direction, which will cause false alarming. While the proposed sparse imaging method can still obtain the focused image even under sparse TOPS mode with reduced PRF [see Fig. 11(d)].

B. Surface Target Simulation

To further validate the designed sparse TOPS mode and the proposed sparse imaging method, we perform several surface target simulations based on the real scenes. Experimental parameters are the same as Table II. Figs. 12 and 13 show the reconstructed images of sea surface and salt pan area by two different imaging methods in conventional TOPS and designed sparse TOPS modes, respectively. Similar to the results in point targets simulation, it can be seen that in sparse TOPS mode, due to the lack of data, the recovered images of two-step algorithm are defocused with obvious ambiguity and energy dispersion along the azimuth direction. Especially the ship targets with high target-to-background ratio (TBR) in Fig. 12. While the proposed $L_{2,1}$ -norm regularization-based sparse imaging method still can achieve the unambiguous recovery of the surveillance region even from the data collected based on the reduced PRF in sparse TOPS mode.

C. Quantitative Analysis

To further quantitatively compare the quality of the images recovered by different methods, we introduce target-to-ambiguity ratio (TAR) and TBR to evaluate the ambiguity and noise suppression ability of two-step algorithm and the proposed method, which are defined as

$$\text{TAR} \triangleq 10 \log_{10} \left(\frac{\sum_{(np,nq) \in \mathcal{I}} |\mathbf{X}(np, nq)|^2}{\sum_{(np,nq) \in \mathcal{A}_i} |\mathbf{X}(np, nq)|^2} \right) \quad (31)$$

and

$$\text{TBR} \triangleq 10 \log_{10} \left(\frac{\sum_{(np,nq) \in \mathcal{T}} |\mathbf{X}(np, nq)|^2}{\sum_{(np,nq) \in \mathcal{B}} |\mathbf{X}(np, nq)|^2} \right) \quad (32)$$

where \mathcal{I} denotes the main imaging area, \mathcal{A}_i is the i th azimuth ambiguity area ($i \in \mathbb{Z}^-$ and $i \in \mathbb{Z}^+$ represent the shifting indexes of ambiguity areas in the left and right sides of the main imaging area, respectively), and \mathcal{B} indicates the background region around the target area \mathcal{T} . The TAR and TBR values of the recovered images in Fig. 12 (marked by yellow box) are shown in Tables III and IV, respectively. From Table III, it is seen that compared with MF-based algorithm, the proposed method can effectively suppress the azimuth ambiguity in sparse TOPS mode, which makes the accurate sparse reconstruction possible. In addition, as shown Table IV, it is found that the

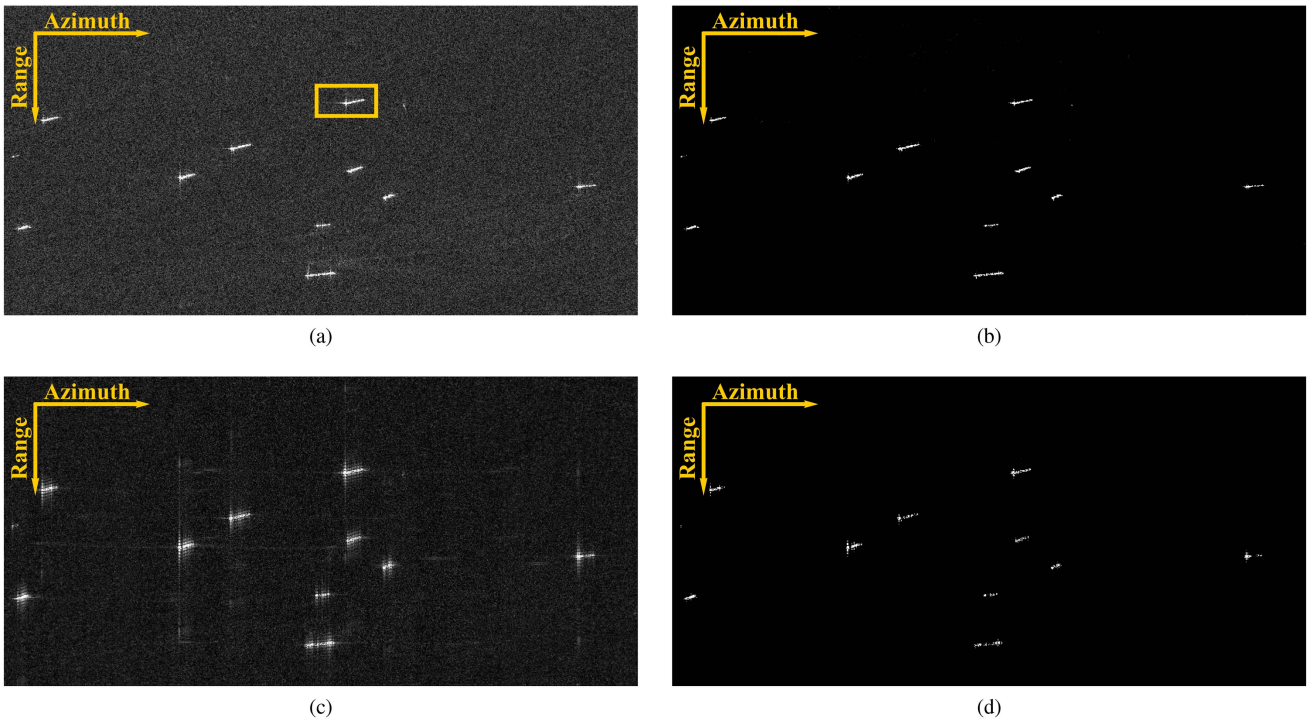


Fig. 12. Reconstructed images of sea surface area by different methods. (a) Two-step algorithm in conventional TOPS mode. (b) Proposed $L_{2,1}$ -norm regularization based sparse imaging method in conventional TOPS mode. (c) Two-step algorithm in sparse TOPS mode. (d) Proposed $L_{2,1}$ -norm regularization-based sparse imaging method in sparse TOPS mode.

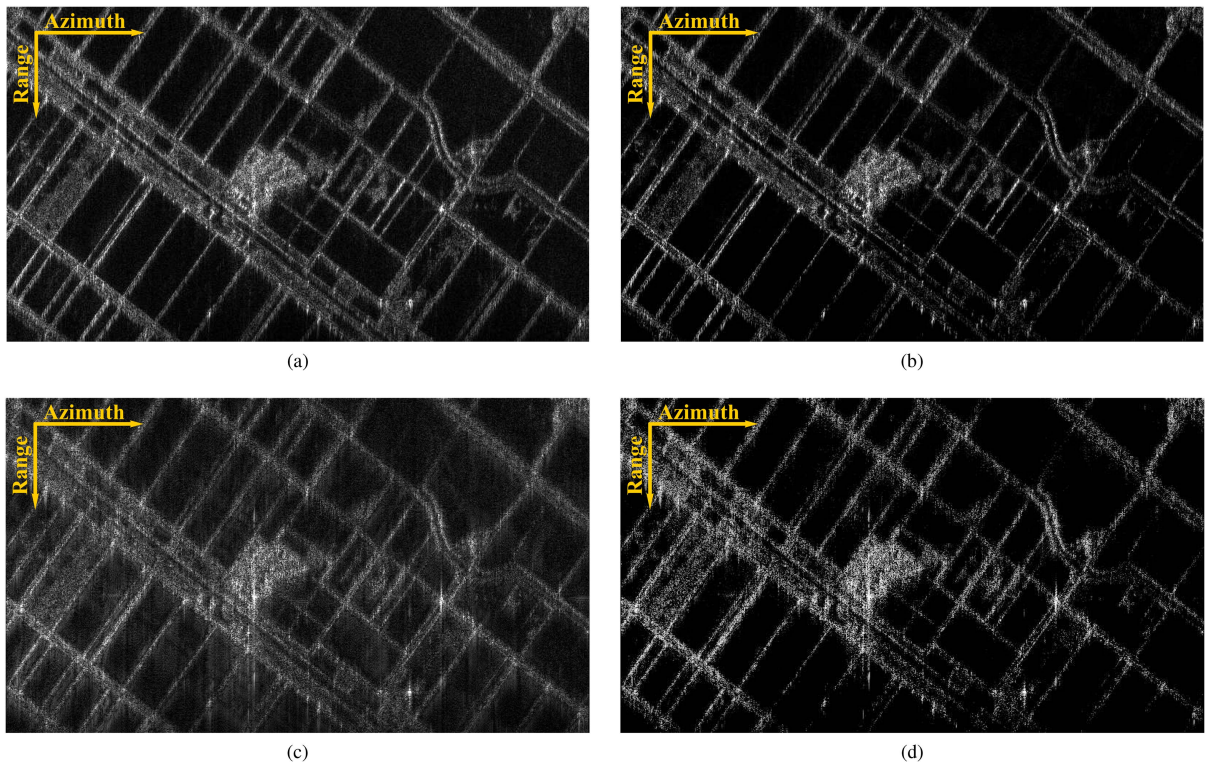


Fig. 13. Reconstructed image of salt pan area by different methods. (a) Two-step algorithm in conventional TOPS mode. (b) Proposed $L_{2,1}$ -norm regularization-based sparse imaging method in conventional TOPS mode. (c) Two-step algorithm in sparse TOPS mode. (d) Proposed $L_{2,1}$ -norm regularization based sparse imaging method in sparse TOPS mode.

TABLE III

TAR VALUE OF EACH AMBIGUITY AREA IN THE RECOVERED IMAGES OF DIFFERENT METHODS IN SPARSE TOPS MODE IN FIG. 12 [dB] (MARKED BY YELLOW BOX)

	$i = 1$	$i = -1$
Two-step algorithm [see Fig. 12(c)]	13.65	14.38
Proposed method (Fig. 12(d))	41.71	47.76

TABLE IV

TBR VALUE OF THE RECOVERED IMAGES OF DIFFERENT METHODS IN SPARSE TOPS MODE IN FIG. 12 [dB] (MARKED BY YELLOW BOX)

	Conventional TOPS	Sparse TOPS
Two-step algorithm [see Fig. 12(c)]	6.92	9.87
Proposed method (Fig. 12(d))	35.13	41.77

proposed method can improve the quality of the recovered image by reducing TBR approximately 32 dB. This means that it effectively removes the noise and clutter in sparse TOPS mode.

VII. CONCLUSION

In this article, we design a novel sparse TOPS SAR imaging mode that combines the advantages of sparse imaging and TOPS. Different from conventional TOPS, this novel mode can improve the swath coverage by reducing the value of PRF. In addition, in order to achieve the unambiguous imaging of this designed mode, an $L_{2,1}$ -norm regularization based sparse TOPS SAR imaging method is introduced to the data processing of down-sampled echo data. The results of system performance analysis show that when PRF is reduced to 75% of original, the designed sparse mode can increase the swath width to 1.33 of the conventional TOPS, and effectively suppress the effect of steering angle on DTAR. In addition, unlike typical MF based algorithm, the proposed sparse imaging method can effectively realize the data processing of the designed mode, and obtain the high-quality image with less noise and clutter. The work in this article provides a new research direction based on sparse signal processing for high-quality and wide-swath imaging.

REFERENCES

- [1] J. C. Curlander and R. N. McDonough, *Synthetic Aperture Radar: Systems and Signal Processing*. New York, NY, USA: Wiley, 1991.
- [2] A. Freeman et al., "The 'myth' of the minimum SAR antenna area constraint," *IEEE Trans. Geosci. Remote Sens.*, vol. 38, no. 1, pp. 320–324, Jan. 2000.
- [3] N. Gebert, G. Krieger, and A. Moreira, "Digital beamforming on receive: Techniques and optimization strategies for high-resolution wide-swath SAR imaging," *IEEE Trans. Aerosp. Electron. Syst.*, vol. 45, no. 2, pp. 564–592, Apr. 2009.
- [4] N. Gebert, F. Q. de Almeida, and G. Krieger, "Airborne demonstration of multichannel SAR imaging," *IEEE Geosci. Remote Sens. Lett.*, vol. 8, no. 5, pp. 963–967, Sep. 2011.
- [5] G. Krieger, N. Gebert, and A. Moreira, "Unambiguous SAR signal reconstruction from nonuniform displaced phase center sampling," *IEEE Geosci. Remote Sens. Lett.*, vol. 1, no. 4, pp. 260–264, Oct. 2004.
- [6] J. Mittermayer, T. Kraus, P. López-Dekker, P. Prats-Iraola, G. Krieger, and A. Moreira, "Wrapped staring spotlight SAR," *IEEE Trans. Geosci. Remote Sens.*, vol. 54, no. 10, pp. 5745–5764, Oct. 2016.
- [7] W. G. Carrara, R. S. Goodman, and R. M. Majewski, *Spotlight Synthetic Aperture Radar: Signal Processing Algorithms*. Norwood, MA, USA: Artech House, 1995.
- [8] A. M. Guarnieri and C. Prati, "ScanSAR focussing and interferometry," *IEEE Trans. Geosci. Remote Sens.*, vol. 34, no. 4, pp. 1029–1038, Jul. 1996.
- [9] A. M. Guarnieri, "ScanSAR interferometric monitoring using the PS technique," in *Proc. ERS/ENVISAT Symp.*, 2000, pp. 1–7.
- [10] F. D. Zan and A. M. Guarnieri, "TOPS: Terrain observation by progressive scan," *IEEE Trans. Geosci. Remote Sens.*, vol. 44, no. 9, pp. 2352–2360, Sep. 2006.
- [11] A. Meta, J. Mittermayer, P. Prats, R. Scheiber, and U. Steinbrecher, "TOPS imaging with TerraSAR-X: Mode design and performance analysis," *IEEE Trans. Geosci. Remote Sens.*, vol. 48, no. 2, pp. 759–769, Feb. 2010.
- [12] J. Mittermayer, R. Lord, and E. Borner, "Sliding spotlight SAR processing for TerraSAR-X using a new formulation of the extended chirp scaling algorithm," in *Proc. Int. Geosci. Remote Sens. Symp.*, 2003, pp. 1462–1464.
- [13] W. Xu, Y. Deng, P. Huang, and R. Wang, "Full-aperture SAR data focusing in the spaceborne squinted sliding-spotlight mode," *IEEE Trans. Geosci. Remote Sens.*, vol. 52, no. 8, pp. 4596–4607, Aug. 2014.
- [14] D. Aria, F. D. Zan, D. Giudici, A. M. Guarnieri, and F. Rocca, "Burst-mode SAR for wide-swath surveys," *Can. J. Remote Sens.*, vol. 33, no. 1, pp. 27–38, Feb. 2007.
- [15] R. Werninghaus and S. Buckkru, "The TerraSAR-X mission and system design," *IEEE Trans. Geosci. Remote Sens.*, vol. 48, no. 2, pp. 606–614, Feb. 2010.
- [16] A. Meta, P. Prats, U. Steinbrecher, R. Scheiber, and U. Steinbrecher, "TerraSAR-X TOPS and ScanSAR comparison," in *Proc. 7th Eur. Conf. Synthetic Aperture Radar*, 2008, pp. 1–4.
- [17] P. Huang and W. Xu, "A new spaceborne burst synthetic aperture radar imaging mode for wide swath coverage," *Remote Sens.*, vol. 6, no. 1, pp. 801–814, Jun. 2014.
- [18] W. Xu, P. Huang, R. Wang, and Y. Deng, "Processing of multi-channel sliding spotlight and TOPS synthetic aperture radar data," *IEEE Trans. Geosci. Remote Sens.*, vol. 51, no. 8, pp. 4417–4429, Aug. 2013.
- [19] I. G. Cumming and F. H. Wong, *Digital Processing of Synthetic Aperture Radar Data: Algorithms and Implementation*. Norwood, MA, USA: Artech House, 2004.
- [20] R. K. Raney, H. Runge, R. Bamler, I. G. Cumming, and F. H. Wong, "Precision SAR processing using chirp scaling," *IEEE Trans. Geosci. Remote Sens.*, vol. 32, no. 4, pp. 786–799, Jul. 1994.
- [21] O. Loffeld, A. Hein, and F. Schneider, "SAR focusing: Scaled inverse fourier transformation and chirp scaling," in *Proc. Int. Geosci. Remote Sens. Symp.*, 1998, pp. 630–632.
- [22] D. P. Belcher and C. J. Baker, "High resolution processing of hybrid stripmap/spotlight mode SAR," *Proc. Inst. Elect. Eng. Radar Sonar Navigat.*, vol. 143, no. 6, pp. 366–374, Jul. 1996.
- [23] J. Mittermayer, A. Moreira, and O. Loffeld, "Spotlight SAR data processing using the frequency scaling algorithm," *IEEE Trans. Geosci. Remote Sens.*, vol. 37, no. 5, pp. 2198–2214, Sep. 1999.
- [24] A. Moreira, J. Mittermayer, and R. Scheiber, "Extended chirp scaling algorithm for air and spaceborne SAR data processing in stripmap and ScanSAR imaging modes," *IEEE Trans. Geosci. Remote Sens.*, vol. 34, no. 5, pp. 1123–1136, Sep. 1996.
- [25] P. Prats, R. Scheiber, J. Mittermayer, A. Meta, and A. Moreira, "Processing of sliding spotlight and TOPS SAR data using baseband azimuth scaling," *IEEE Trans. Geosci. Remote Sens.*, vol. 48, no. 2, pp. 770–780, Feb. 2010.
- [26] W. Xu and Y. Deng, "An imaging approach for TOPSSAR data based on azimuth pre-processing and post-processing," *J. Inf. Technol.*, vol. 33, no. 4, pp. 798–804, Apr. 2011.
- [27] X. Bai, J. Sun, W. Hong, and S. Mao, "On the TOPS mode spaceborne SAR," *Sci. China Inf. Sci.*, vol. 53, no. 2, pp. 367–378, Feb. 2010.
- [28] G. Engen and Y. Larsen, "Efficient full aperture processing of TOPS mode data using the moving band chirp z-transform," *IEEE Trans. Geosci. Remote Sens.*, vol. 49, no. 10, pp. 3688–3693, Oct. 2011.
- [29] W. Xu, P. Huang, Y. Deng, J. Sun, and X. Shang, "An efficient approach with scaling factors for TOPS-mode SAR data focusing," *IEEE Geosci. Remote Sens. Lett.*, vol. 8, no. 5, pp. 929–933, Sep. 2011.
- [30] W. Xu, P. Huang, R. Wang, Y. Deng, and Y. Lu, "TOPS mode raw data processing using chirp scaling algorithm," *IEEE J. Sel. Topics Appl. Earth Observ. Remote Sens.*, vol. 7, no. 1, pp. 235–246, Jan. 2014.
- [31] R. G. Baraniuk, E. Candes, M. Elad, and Y. Ma, "Applications of sparse representation and compressive sensing," *Proc. IEEE*, vol. 98, no. 6, pp. 906–909, Jun. 2010.
- [32] D. L. Donoho, "Compressed sensing," *IEEE Trans. Inf. Theory*, vol. 52, no. 4, pp. 1289–1306, Apr. 2006.

- [33] E. J. Candes and T. Tao, "Near-optimal signal recovery from random projections: Universal encoding strategies?," *IEEE Trans. Inf. Theory*, vol. 52, no. 12, pp. 5406–5425, Dec. 2006.
- [34] H. Nyquist, "Certain topics in telegraph transmission theory," *Trans. Amer. Inst. Elect. Eng.*, vol. 47, no. 2, pp. 617–644, Apr. 1928.
- [35] C. E. Shannon, "Communication in the presence of noise," *Proc. Inst. Radio Eng.*, vol. 37, no. 1, pp. 10–21, Jan. 1949.
- [36] E. J. Candes, J. K. Romberg, and T. Tao, "Stable signal recovery from incomplete and inaccurate measurements," *Commun. Pure Appl. Math.*, vol. 59, no. 8, pp. 1207–1223, 2006.
- [37] B. Zhang, W. Hong, and Y. Wu, "Sparse microwave imaging: Principles and applications," *Sci. China Inf. Sci.*, vol. 55, no. 8, pp. 1722–1754, Aug. 2012.
- [38] J. Fang, Z. Xu, B. Zhang, W. Hong, and Y. Wu, "Fast compressed sensing SAR imaging based on approximated observation," *IEEE J. Sel. Topics Appl. Earth Observ. Remote Sens.*, vol. 7, no. 1, pp. 352–363, Jan. 2014.
- [39] H. Bi, B. Zhang, X. Zhu, and W. Hong, "Azimuth-range decouple-based L_1 regularization method for wide ScanSAR imaging via extended chirp scaling," *J. Appl. Remote Sens.*, vol. 11, no. 1, Jan. 2017, Art. no. 015007.
- [40] Z. Xu, Z. Wei, C. Wu, and B. Zhang, "Multichannel sliding spotlight SAR imaging based on sparse signal processing," in *Proc. Int. Geosci. Remote Sens. Symp.*, 2018, pp. 3703–3706.
- [41] Y. Wang, Z. Ding, P. Xu, K. Chen, T. Zeng, and T. Long, "Strip layering diagram-based optimum continuously varying pulse interval sequence design for extremely high-resolution spaceborne sliding spotlight SAR," *IEEE Trans. Geosci. Remote Sens.*, vol. 59, no. 8, pp. 6751–6770, Aug. 2021.
- [42] H. Bi, B. Zhang, X. Zhu, C. Jiang, and W. Hong, "Extended chirp scaling-baseband azimuth scaling-based azimuth-range decouple L_1 regularization for TOPS SAR imaging via CAMP," *IEEE Trans. Geosci. Remote Sens.*, vol. 55, no. 7, pp. 3748–3763, Jul. 2017.
- [43] M. Herman and T. Strohmer, "High-resolution radar via compressed sensing," *IEEE Trans. Signal Process.*, vol. 57, no. 6, pp. 2275–2284, Jun. 2009.
- [44] B. Zhang, Z. Zhang, C. Jiang, W. Hong, and Y. Wu, "System design and first airborne experiment of sparse microwave imaging radar: Initial results," *Sci. China Inf. Sci.*, vol. 58, no. 6, pp. 1–10, Jun. 2015.
- [45] H. Bi, G. Bi, B. Zhang, W. Hong, and Y. Wu, "From theory to application: Real-time sparse SAR imaging," *IEEE Trans. Geosci. Remote Sens.*, vol. 58, no. 4, pp. 2928–2936, Apr. 2020.
- [46] H. Bi, X. Lu, Y. Yin, W. Yang, and D. Zhu, "Sparse SAR imaging based on periodic block sampling data," *IEEE Trans. Geosci. Remote Sens.*, vol. 60, pp. 1–12, 2022.



Hui Bi (Member, IEEE) was born in Shandong, China, in 1991. He received the bachelor's degree in electronics and information engineering from YanTai University, Yantai, China, in 2012, and the Ph.D. degree in signal and information processing from the University of Chinese Academy of Sciences (UCAS), Beijing, China, in 2017.

From 2012 to 2017, he was with the Science and Technology on Microwave Imaging Laboratory, Institute of Electronics, Chinese Academy of Sciences (IECAS), Beijing, China. He was a Research Fellow

with the School of Electrical and Electronic Engineering, Nanyang Technological University (NTU), Singapore, from 2017 to 2018. Since 2018, he has been with the College of Electronic and Information Engineering, Nanjing University of Aeronautics and Astronautics (NUAA), Nanjing, China, where he is currently a Professor. His main research interests include sparse microwave imaging with compressive sensing, synthetic aperture radar data processing and application, sparse signal processing, and 3-D/4-D SAR imaging.



Guoxu Li was born in Shandong, China, in 1998. He received the bachelor's degree in electronics and information engineering from the Shandong Jiaotong University, Jinan, China, in 2021. He is currently working toward the master's degree in electronic information with the Nanjing University of Aeronautics and Astronautics, Nanjing, China.

His current research interests include sparse synthetic aperture radar (SAR) mode design and SAR imaging.



Yufan Song was born in Hebei, China, in 1999. She received the bachelor's degree in electronics and information engineering from the University of Electronic Science and Technology of China, Chengdu, China, in 2020. She is currently working toward the Ph.D. degree in information and communication engineering with the Nanjing University of Aeronautics and Astronautics, Nanjing, China.

Her current research interests include sparse microwave imaging, synthetic aperture radar data processing, and their applications



Jingjing Zhang was born in Anhui, China, in 1986. He received the B.E. degree in electronic information engineering from the University of Science and Technology of China (USTC), Anhui, China, in 2009 and the Doctor of Engineering degree in signal and information processing from the University of Chinese Academy of Sciences (UCAS), Beijing, China, in 2017.

From 2017 to 2021, he was with the School of Information Science and Technology, Fudan University, Shanghai, China. Since 2021, he has been with

the College of Electronics and Information Engineering, Nanjing University of Aeronautics and Astronautics, Nanjing, China, as an Associate Professor. His research interests include the design, modeling and calibration of polarimetric SAR systems; SAR imaging; and polarimetric and polarimetric interferometric SAR signal processing and applications.



Daiyin Zhu was born in Wuxi, China, in 1974. He received the B.S. degree in electronic engineering from Southeast University, Nanjing, China, in 1996 and the M.S. and Ph.D. degrees in electronics from the Nanjing University of Aeronautics and Astronautics (NUAA), Nanjing, China, in 1998 and 2002, respectively.

From 1998 to 1999, he was a Guest Scientist with the Institute of Radio Frequency Technology, German Aerospace Center (DLR), Oberpfaffenhofen, Germany. In 1998, he joined the Department of Electronic Engineering, NUAA, where he is currently a Professor. His current

research interests include radar imaging algorithms, SAR ground moving target indication, SAR/ISAR autofocus techniques, and SAR interferometry.



Wen Hong (Senior Member, IEEE) was born in 1968. She received the Ph.D. degree in communication and electronic system from Beihang University, Beijing, China, in 1997.

She was with the Department of Electrical Engineering, Beihang University, as a Faculty Member in signal and information processing from 1997 to 2002. In between, she was with the DLR-HF, Wessling, Germany, as a Guest Scientist from 1998 to 1999. Since 2002, she has been working in the Institute of Electronics, Chinese Academy of Sciences (IECAS),

where she is currently a Professor. Her main research interests are polarimetric/polarimetric interferometric synthetic aperture radar data processing and application, 3-D SAR signal processing, circular SAR signal processing, and sparse microwave imaging.



Yirong Wu received the M.S. degree in electronic engineering from the Beijing Institute of Technology, Beijing, China, in 1988 and the Ph.D. degree in information and communication engineering from the Institute of Electronics, Chinese Academy of Sciences (IECAS), Beijing, China, in 2001.

He is currently with the Dean and Professor of the Aerospace Information Research Institute, Chinese Academy of Sciences. He has more than 30 years of experience in remote sensing processing system design. His current research interests include microwave

imaging, signal and information procession, and related applications.